

Short gamma-ray burst progenitors have short delay times

M. Pracchia¹ and O. S. Salafia^{2,3}

¹ STAR Institute, Université de Liège, Sart Tilman B4000 Liège, Belgium

² INAF – Osservatorio Astronomico di Brera, via Emilio Bianchi 46, I-23807 Merate (LC), Italy

³ INFN – sezione di Milano-Bicocca, Piazza della Scienza 3, I-20126 Milano (MI), Italy

Received xxx; accepted xxx

ABSTRACT

Short gamma-ray bursts (SGRBs) are thought to be primarily associated with binary neutron star (BNS) mergers. The SGRB population can therefore be scrutinized to look for signatures of the delay time between the formation of the progenitor massive star binary and the eventual merger, which could produce an evolution of the cosmic rate density of such events whose shape departs from that of the cosmic star formation history (CSFH). To that purpose, we study a large sample of SGRBs within a hierarchical Bayesian framework, with a particular focus on the delay time distribution (DTD) of the population. Following previous studies, we model the DTD either as a power-law with a minimum time delay or as a log-normal function. We consider two models for the intrinsic SGRB luminosity distribution: an empirical luminosity function (ELF) with a doubly broken power-law shape, and one based on a quasi-universal structured jet (QUSJ) model. Regardless of the chosen parametrization, we find average time delays $10 \lesssim \langle \tau_d \rangle / \text{Myr} \lesssim 800$ and a minimum delay time $\tau_{d,\min} \lesssim 350 \text{ Myr}$, in contrast with previous studies that found long delay times of few Gyr. We demonstrate that the cause of the longer inferred time delays in past studies most likely resides in an incorrect treatment of selection effects.

Key words. relativistic astrophysics – gamma-ray bursts: general – gamma-ray burst: individual: GRB 221009A – stars: circumstellar matter

1. Introduction

Gamma-ray bursts (GRBs) are high energy gamma-ray transients of astrophysical origin. These are thought to be produced as a result of cataclysmic astrophysical events and they are commonly classified according to their time duration and spectral hardness (Kouveliotou et al. 1993; von Kienlin et al. 2020): short GRBs (SGRBs) are shorter in time duration and on average harder in energy spectrum compared to long GRBs (LGRBs). While a sizable number of LGRBs have been solidly associated with extreme cases of core-collapse supernovae (CC-SNe), SGRBs are believed to be mainly associated with compact binary coalescence (CBC) events, namely binary neutron star (BNS) or neutron star-black hole (NSBH) mergers (Berger 2014). This connection was cemented by the joint observation and unambiguous association of GRB 170817A and the gravitational wave (GW) signal GW170817 from a BNS merger (Abbott et al. 2017).

Studies of the SGRB population generally aim to study the intrinsic luminosity distribution (also known as ‘luminosity function’) of those events, inferring its parameters from a sample of GRBs observed at cosmological distances by various instruments. While some studies describe the luminosity distribution as an empirically defined function (Wanderman & Piran 2015, hereafter W15; Ghirlanda et al. 2016, hereafter G16), others test the structured jet hypothesis utilizing more physically motivated models to describe the emitted luminosity (Tan & Yu 2020; Salafia et al. 2023, hereafter S23).

Bearing in mind the CBC origin scenario, the cosmological rate density evolution of the SGRB population depends on the time needed by the compact objects to form from massive stars and for the binary system to merge. Simple theoretical considerations for a BNS system whose orbital separation shrinks due to

gravitational radiation suggest that time delays (τ_d) between the star formation and the merger should be distributed as a power-law $dP/d\tau_d \propto \tau_d^{-\alpha_\tau}$ with $\alpha_\tau \sim 1$ (Piran 1992). This model has been widely used in SGRB population studies (e.g. Paul 2018, Tan & Yu 2020, W15). For example, W15, studying a sample of SGRBs detected by *Fermi*/GBM, *Swift*/BAT and *CGRO*/BATSE, found a delay-time distribution (DTD) power-law index $\alpha_\tau \sim 1$, keeping the minimum time delay fixed at $\tau_d^{\min} = 20 \text{ Myr}$. Some works suggest, though, that the power-law index of the DTD might be steeper, leading to shorter coalescence times. D’Avanzo et al. (2014), for example, selected a sample of *Swift*/BAT using quality cuts that maximize the probability of a redshift measurement and found that its DTD is best represented by $\alpha_\tau \sim 1.5$ and $\tau_d^{\min} = 10 \text{ Myr}$. More recent studies of the association between SGRB events with their host galaxies (Zevin et al. 2022) also inferred a steeper power-law DTD, with $\alpha_\tau \sim 1.5 – 2.2$, but with larger minimum time delays $\tau_d^{\min} \sim 105 – 250 \text{ Myr}$. An analysis of the chemical enrichment of r-process heavy elements in the Milky Way, on the other hand, under the assumption that they are mostly generated in BNS mergers, finds that fast mergers are required, with $\alpha_\tau \gtrsim 2.0$ and $\tau_{\min} \lesssim 40 \text{ Myr}$ (Chen et al. 2025).

Another widely adopted model of the SGRB DTD is a log-normal distribution $dP/d\tau_d = \exp[-1/2(\ln \tau_d - \ln \mu_\tau)^2/2\sigma_\tau^2]/\sigma_\tau \tau_d \sqrt{2\pi}$, for which W15 finds $\mu_\tau \sim 3 – 4 \text{ Gyr}$ and $\sigma_\tau \lesssim 0.2$. Similar values are reported by Luo et al. (2022), where a simulated SGRB population with a structured jet model fitting with the observed *Fermi*/GBM photon flux distribution is shown to be compatible with a log-normal DTD, disfavoring power-law and Gaussian DTD models.

Some works find different evolution branches for the BNS population, which can correspond to different BNS formation channels. Studies of BNS systems in our Galaxy show that

the BNS population might be composed of two distinct sub-populations: a ‘fast’ one, with either a power-law DTD with $\alpha_\tau \sim 2$ (Maoz & Nakar 2025) or a log-normal one with $\mu_\tau \sim 300$ Myr and $\sigma_\tau \sim 1$ (Beniamini & Piran 2019), and a ‘slow’ one, with τ_d typically above Gyr, and with $\alpha_\tau \sim 1$. In particular, Maoz & Nakar (2025) estimates that within Galactic BNS systems that merge within a Hubble time, the fast component is $\sim 10 - 100$ times more abundant than the slow one. Beniamini & Piran (2019) reach the similar, but slightly weaker conclusion that almost half of the Milky Way BNS population must belong to the fast-merging channel. Multi-band optical and near-infrared observations of SGRB host galaxies aimed to measure their stellar masses and population ages (Leibler & Berger 2010) show a similar duality where long ($\tau_d \sim 3$ Gyr) and short time delays ($\tau_d \sim 0.2$ Gyr) are associated, respectively, with early and late-type galaxies.

In this paper we perform a study of the SGRB population, assuming two different models of the DTD and two distinct models of the luminosity function, to test for the robustness of our conclusions. The parameters are inferred within a hierarchical Bayesian framework (Mandel et al. 2019, hereafter M19).

In Sect. 2 we describe our methodology and sample selection. Results are shown in Sect. 3 and discussed in Sect. 4, where we also demonstrate a few possible sources of biases and we analyze their impact on the parameters inference of our population.

2. Methods

2.1. Bayesian hierarchical inference method

Our approach to characterize the SGRB population follows closely S23, with some updates that we describe below. The parameters of the population model (formally called ‘hyper-parameters’) constitute the elements of the hyper-parameter vector λ'_{pop} . Each SGRB is described by a vector of source parameters $\lambda'_{\text{src},i}$, which are estimated based on the measured data \mathbf{d}_i (here $i = 1, \dots, N_{\text{obs}}$ and N_{obs} is the number of events in the sample). Following Eqs. 7 and 8 in M19, the posterior probability distribution function (PDF) can be written as

$$P(\lambda'_{\text{pop}}|\{\mathbf{d}_i\}) = \frac{\pi(\lambda'_{\text{pop}})P(\{\mathbf{d}_i\}|\lambda'_{\text{pop}})}{P(\{\mathbf{d}_i\})} = \frac{\pi(\lambda'_{\text{pop}})}{P(\{\mathbf{d}_i\})} \prod_{i=1}^{N_{\text{obs}}} \frac{N_i(\mathbf{d}_i|\lambda'_{\text{pop}})}{\mathcal{D}(\lambda'_{\text{pop}})}. \quad (1)$$

Here $\pi(\lambda'_{\text{pop}})$ is the ‘hyper-prior’, that is, the joint prior on the hyper-parameters, and $P(\{\mathbf{d}_i\})$ is the Bayesian evidence of the data (in practice, a normalization constant). The likelihood of the data given the hyper-parameters, $P(\{\mathbf{d}_i\}|\lambda'_{\text{pop}})$ is written as a product of single-source terms, each of which is expressed as a ratio of a numerator over a denominator, being respectively

$$N_i(\mathbf{d}_i|\lambda'_{\text{pop}}) = \int P(\mathbf{d}_i|\lambda_{\text{src}})P_{\text{pop}}(\lambda_{\text{src}}|\lambda'_{\text{pop}})d\lambda_{\text{src}}, \quad (2)$$

and

$$\mathcal{D}(\lambda'_{\text{pop}}) = \int P_{\text{det}}(\lambda_{\text{src}})P_{\text{pop}}(\lambda_{\text{src}}|\lambda'_{\text{pop}})d\lambda_{\text{src}}. \quad (3)$$

Here $P_{\text{pop}}(\lambda_{\text{src}}|\lambda'_{\text{pop}})$ is the ‘population probability’ that specifies the probability density of the source parameters for any choice of the hyper-parameters; $P_{\text{det}}(\lambda_{\text{src}})$ is the selection function: it represents the probability that an event with source parameters λ_{src} , sampled from the population, is selected and hence included in

the sample. The selection function therefore contains all information on selection effects, that stem both from the detection process and also from any additional selection cuts that define the sample; $P(\mathbf{d}_i|\lambda_{\text{src}})$ is the likelihood of measuring the data for a single event given the source parameters. This framework has been implemented in the publicly available `grbpop` code¹, which we use as a starting point to implement different SGRB population models.

2.2. Including the observed number of events in the inference

In order to take into account the information on the number of events in the sample and hence to include the SGRB local rate density R_0 as one of the parameters of the population, we updated the definition of our posterior probability by embedding the Poissonian probability of the number of observed events. Following Eq. 11 in M19, given the total rate of astrophysical events in a population

$$R(\lambda_{\text{pop}}) = \int_0^\infty \frac{\dot{\rho}(z, \lambda_{\text{pop}})}{1+z} \frac{dV}{dz} dz \quad (4)$$

with $\lambda_{\text{pop}} \equiv (\lambda'_{\text{pop}}, R_0)$, the number of expected detections for a sample of a given detector is

$$N_{\text{det}}(\lambda_{\text{pop}}) = \eta_{\text{DC}} \cdot T \cdot R(\lambda_{\text{pop}}) \cdot \mathcal{D}(\lambda'_{\text{pop}}), \quad (5)$$

where η_{DC} is the product of the detector duty cycle times the average fraction of the sky accessible to it², $R(\lambda_{\text{pop}})$ is the total cosmic rate of events, T is the duration of the observation period and $\mathcal{D}(\lambda'_{\text{pop}})$ is the term defined in Eq. 3, which can be shown to be equivalent to the fraction of events in the population that pass the detection and selection cuts. The probability of observing N_{obs} events given $N_{\text{det}}(\lambda_{\text{pop}})$ is then a Poissonian probability, and the posterior PDF becomes

$$P(\lambda_{\text{pop}}|\{\mathbf{d}_i\}) = \frac{\pi(\lambda'_{\text{pop}})}{P(\{\mathbf{d}_i\})} \prod_{i=1}^{N_{\text{obs}}} \left[\frac{N_i(\mathbf{d}_i|\lambda'_{\text{pop}})}{\mathcal{D}(\lambda'_{\text{pop}})} \right] e^{-N_{\text{det}}(N_{\text{det}})^{N_{\text{obs}}}}, \quad (6)$$

where the $\frac{1}{N_{\text{obs}}!}$ term is omitted due to the distinguishability of the events in the sample (M19).

We define the isotropic equivalent of the peak luminosity $L(p_{[E_0, E_1]}, E_p, z)$ following Eq. 17 in S23 and modeling the SGRB photon spectrum as a power-law with an exponential cut-off Ghirlanda et al. (2004), with the low-energy photon index set to the median value of α from the spectral analysis of the *Fermi*/GBM SGRB catalog (S23).

2.3. Population models

2.3.1. Rate density evolution

Guided by the expectation that short GRBs are generated mainly in compact binary mergers, like BNS or NSBH systems, the redshift probability distribution is modeled considering a fixed cosmic star formation history (CSFH) and convolving it with the distribution of time delays τ_d between the binary system formation and the eventual merger. Two delay-time distribution (DTD)

¹ <https://github.com/omsharansalafia/grbpop>, see S23.

² The term η_{DC} in general expresses the fraction of events that pass any pre-selection that does not depend on the properties of the source and is not accounted for in the P_{det} selection effects model.

models are considered: the first is a power law with a minimum time delay cut-off, namely

$$P(\tau_d | \lambda'_{\text{pop}}) \propto \begin{cases} 0, & \tau_d < \tau_d^{\min}; \\ \tau_d^{-\alpha_\tau}, & \tau_d \geq \tau_d^{\min}, \end{cases} \quad (7)$$

where the free parameters are τ_d^{\min} and the index α_τ , the second is a log-normal DTD, that is

$$P(\tau_d | \lambda'_{\text{pop}}) = \exp \left[-\frac{1}{2} \left(\frac{\ln \tau_d - \ln \mu_\tau}{\sigma_\tau} \right)^2 \right] (\tau_d \sqrt{2\pi\sigma_\tau^2})^{-1}, \quad (8)$$

where the parameters to constrain are the median value μ_τ and the dispersion σ_τ . The rate density distribution is therefore

$$\dot{\rho}(z, \lambda'_{\text{pop}}) \propto \int_z^\infty \psi(z) P(t_{\text{LB}}(z') - t_{\text{LB}}(z) | \lambda'_{\text{pop}}) \frac{dt}{dz'} dz', \quad (9)$$

where $\psi(z)$ is the CSFH and $t_{\text{LB}}(z)$ is the cosmological look-back time at redshift z . We choose to adopt the CSFH model from [Madau & Fragos \(2017\)](#),

$$\psi(z) \propto \frac{(1+z)^{a_\psi}}{1 + \left(\frac{1+z}{1+z_\psi} \right)^{b_\psi}} \quad (10)$$

with $a_\psi = 2.6$, $b_\psi = 6.2$ and $z_\psi = 2.2$. The redshift probability distribution of SGRBs is then computed as

$$P(z | \lambda'_{\text{pop}}) \propto \frac{\dot{\rho}(z, \lambda'_{\text{pop}}) dV}{1+z} \frac{dz}{dV}, \quad (11)$$

where dV/dz is the differential comoving volume at redshift z .

2.3.2. Luminosity function models: ELF and QUSJ

To describe the luminosity function (i.e., the luminosity PDF) of our population, we chose two different models. The first one, to which we refer as the ‘empirical luminosity function’ model (ELF hereafter), is based on a doubly broken power law luminosity function, extending the [W15](#) luminosity function model to lower luminosities. Following³ [Abbott et al. \(2022\)](#), we express the luminosity function in this model as

$$P(L | \lambda'_{\text{pop}}) \propto \begin{cases} 0, & L < L_0; \\ \left(\frac{L}{L_*} \right)^{-\alpha_{\text{BPL}}-1} \left(\frac{L}{L_{**}} \right)^{-\gamma_{\text{BPL}}-1}, & L_0 \leq L \leq L_{**}; \\ \left(\frac{L}{L_*} \right)^{-\alpha_{\text{BPL}}-1}, & L_{**} < L \leq L_*; \\ \left(\frac{L}{L_*} \right)^{-\beta_{\text{BPL}}-1}, & L > L_*. \end{cases} \quad (12)$$

Here L_0 , L_{**} and L_* are the minimum luminosity, low-luminosity break and high-luminosity break, respectively. The power law indices of the three branches are expressed through the γ_{BPL} , α_{BPL} and β_{BPL} parameters, to facilitate the comparison with [Abbott et al. \(2022\)](#). As a way to incorporate in this model some information from GRB 170817A, we chose our prior on L_0 to ensure

³ We note that the formulation in [Abbott et al. \(2022\)](#), which is inspired to [W15](#), is in terms of the probability density of the logarithm of the luminosity, $dP/d\ln L$, while in our formalism the quantity $P(L | \lambda'_{\text{pop}})$ is a probability density of the luminosity, dP/dL . For that reason, the power law slopes in our formulation are steeper by one with respect to their definition.

that $L_0 < L_{17A}$, where $L_{17A} = 1.2_{-0.4}^{+0.5} \times 10^{47} \text{ erg s}^{-1}$ is the peak luminosity of GRB 170817A ([S23](#)).

In order to fully specify the population properties, the PDF of the peak photon energy E_p of the GRB spectral energy distribution across the population must be also specified. Following [S23](#), we modeled this as a log-normal distribution with a median value that depends on L ,

$$P(E_p | L, \lambda'_{\text{pop}}) = \frac{\exp \left[-\frac{1}{2} \left(\frac{\ln(E_p) - \ln(\tilde{E}_p(L))}{\sigma_c} \right)^2 \right]}{E_p \sqrt{2\pi\sigma_c^2}} \quad (13)$$

where $\tilde{E}_p(L) = E_p^* (L/L_*)^y$ allows for a Yonetoku-like correlation ([Yonetoku et al. 2004](#)) when $y \neq 0$. L and E_p are therefore parametrized with a common probability density $P(L, E_p | \lambda'_{\text{pop}}) = P(E_p | L, \lambda'_{\text{pop}})P(L | \lambda'_{\text{pop}})$.

The second model we considered is the quasi-universal structured jet population model (QUSJ hereafter) from [S23](#), which also features a correlated joint distribution of L and E_p , induced by the jet structure. The latter is defined by two dimensionless functions of the ratio of the viewing angle θ_v to the ‘jet core’ angle θ_c , called $\ell(\theta_v/\theta_c)$ and $\eta(\theta_v/\theta_c)$, that describe how the luminosity and E_p depend on the jet viewing angle (see [S23](#) for more details). In the analysis based on the QUSJ model, we include the information on the luminosity, peak photon energy and viewing angle of GRB 170817A in the form of priors on the population parameters, following [S23](#). In both cases the redshift probability distribution $P(z | \lambda'_{\text{pop}})$ is assumed to be independent of L and E_p . The distribution of source parameters across the population is therefore

$$P_{\text{pop}}(\lambda_{\text{src}} | \lambda'_{\text{pop}}) = P(L, E_p | \lambda'_{\text{pop}})P(z | \lambda'_{\text{pop}}). \quad (14)$$

2.3.3. W15 population model

In order to get some insight on the difference between our results and those of previous studies, we set out to reproduce the [W15](#) constraints using hierarchical Bayesian inference, but with the same sample and selection effects modeling used in that work.

For that purpose, the luminosity probability distribution $P(L | \lambda'_{\text{pop}})$ we employed is the same as in Eq. 12, but fixing $L_0 = L_{**} = 5 \times 10^{49} \text{ erg s}^{-1}$. The parameters to be constrained for $P(L | \lambda'_{\text{pop}})$ therefore are only α_{BPL} , β_{BPL} and L_* .

The redshift probability distribution $P(z | \lambda'_{\text{pop}})$ was modeled as in Sect. 2.3.1. The only difference is for the power-law DTD model, where the minimum time delay was fixed to $\tau_d^{\min} = 20 \text{ Myr}$.

The SGRB photon spectrum $d\dot{N}/dE(E, E_p)$ was modeled as a Band function [Band et al. \(1993\)](#), whose parameters were fixed to $E_p = 800 \text{ keV}$, $\alpha_{\text{Band}} = -0.5$ and $\beta_{\text{Band}} = -2.25$ as in the original paper (motivated by the analysis of [Nava et al. 2011](#)).

Since the spectral energy peak in this model is fixed, the source parameters are only the GRB luminosity and redshift, that is, $\lambda_{\text{src}} = (L, z)$. In Appendix A we give technical details on how this difference is handled in the inference.

2.4. Samples and detection efficiencies

When building our reference SGRB samples, we need to carefully model the selection effects that molded them. We considered therefore two samples for the analysis, built in the same way as in the ‘flux-limited sample analysis’ of [S23](#).

The likelihood numerators $N_i(\mathbf{d}_i|\lambda'_{\text{pop}})$ for each event in the samples and denominators $\mathcal{D}(\lambda'_{\text{pop}})$ are then computed in the same way as in S23 for both the ELF and the QUSJ case, since the only term that changes between the two models is $P_{\text{pop}}(\lambda_{\text{src}}|\lambda'_{\text{pop}})$.

2.4.1. Observer-frame sample

The first sample consists of short GRBs detected by *Fermi*/GBM with publicly available spectral analysis results. We selected events with $T_{90} < 2$ s from the GBM first 10 years of observation, namely from the 12th July 2008 to 11th July 2018. We applied a completeness cut on the 64 ms peak photon flux in the [50 – 300] keV energy band, selecting only the events with $p_{[50,300]} > p_{\text{lim,GBM}} = 3.50 \text{ cm}^{-2} \text{ s}^{-1}$, which is the value above which we can consider our sample as complete in flux (S23). Additional cuts on the observed spectral peak energy $E_{\text{p,obs}}$ were applied, considering only events with best fit values $50 \text{ keV} \leq E_{\text{p,obs}} \leq 10 \text{ MeV}$, which is the spectral range where the effective area of the *Fermi*/GBM detectors is optimal. After all cuts, the sample contains 210 short GRB events. Hereon, we refer to this as the ‘observer-frame sample’.

The detection efficiency for this sample is modeled as

$$P_{\text{det}}(L, E_{\text{p}}, z) = \Theta(p_{[50,300]}(L, E_{\text{p}}, z) - p_{\text{lim,GBM}}) \times \Theta(E_{\text{p}}/(1+z) - 50 \text{ keV}) \Theta(10 \text{ MeV} - E_{\text{p}}/(1+z)), \quad (15)$$

where $\Theta(x)$ is the Heaviside step function.

Given the number of events contained in the observer-frame sample, we consider its event detection rate to estimate the astrophysical local rate density R_0 of the SGRB population. The N_{det} for the Poissonian term in Eq. 6 is therefore computed using the $\mathcal{D}(\lambda'_{\text{pop}})$ for this sample, an observation period of $T = 10$ yr and a multiplicative factor $\eta_{\text{DC}} = 0.59$ accounting for both the accessible field of view and the duty cycle of *Fermi*/GBM (Burns et al. 2016).

2.4.2. Rest-frame sample

The second sample consists of short GRBs detected by *Fermi*/GBM and *Swift*/BAT that pass a set of stringent cuts that maximize the redshift completeness without distorting the redshift distribution. In practice, this is the sub-sample of the S-BAT4ext catalog (Ferro et al. 2023) of events that were also detected by *Fermi*/GBM. The selection includes a *Swift*/BAT completeness flux threshold in the [15 – 150] keV energy band, $p_{[15,150]} > p_{\text{lim,BAT}} = 3.50 \text{ cm}^{-2} \text{ s}^{-1}$, in addition to the same *Fermi*/GBM completeness cuts as in the observer-frame sample. The sample consists of 18 short GRBs events, 16 of which have a measured redshift. For those events we use the results of the spectral analysis performed in S23, which yields, for each event i , a posterior on the source parameters $P(L, E_{\text{p}}, z | \mathbf{d}_i)$, given a prior $\pi(L, E_{\text{p}}, z) \propto (1+z)^{-1} L^{-1}$. We refer to this sample as the ‘rest-frame sample’. We do not use the number of events in this sample to inform our estimate of R_0 , because of the difficulty in modeling correctly the duty cycle factor η_{DC} incorporating all the cuts that define the sample.

Because we require the detection by *Fermi*/GBM, the rest-frame sample detection efficiency includes the same cuts as the observer-frame sample. In addition, it features a factor

$$\Theta(p_{[15,150]}(L, E_{\text{p}}, z) - p_{\text{lim,BAT}}) \quad (16)$$

to account for the *Swift*/BAT completeness cut. All other S-BAT4 cuts are independent on the source properties and hence do not enter the definition of this efficiency.

We note that GRB 170817A is not included in either of these samples, because its peak flux is below the *Fermi*/GBM completeness threshold. In the case of the quasi-universal jet population model, our results still include information on this event in the form of a prior on the hyper-parameters, which we built following the procedure used by S23 in their flux-limited sample analysis.

2.4.3. W15 samples

The observer-frame samples considered for the W15 population analysis consist of short GRBs observed by *Fermi*/GBM, *CGRO*/BATSE and *Swift*/BAT. For the three detectors, the detection efficiency was modeled as an hard threshold on the 64 ms peak photon flux in their respective most sensitive detector energy band as in Eq. 16. The photon flux thresholds considered for *CGRO*/BATSE and *Fermi*/GBM in the $[E_0, E_1] = [50, 300]$ keV detector energy band for this analysis were, respectively, $p_{\text{lim,BATSE}} = 1.5 \text{ cm}^{-2} \text{ s}^{-1}$ and $p_{\text{lim,GBM}} = 2.37 \text{ cm}^{-2} \text{ s}^{-1}$, while for *Swift*/BAT it is $p_{\text{lim,BAT}} = 2.5 \text{ cm}^{-2} \text{ s}^{-1}$ in the $[E_0^{\text{d}}, E_1^{\text{d}}] = [15, 150]$ keV band.

The BATSE and *Fermi* sample contain GRBs with a measured $p_{[E_0, E_1]}$ above the respective detector threshold and $T_{90} < 2$ s. While for BATSE these selection effects have been applied to the entirety of its catalog, for a total of 414 events, the *Fermi*/GBM events were considered up to the 10th of April 2013, as in W15, yielding 146 bursts.

The rest-frame sample was built following W15. The sample contains events detected by *Swift*/BAT with measured redshift and L , with $T_{90} < 2$ s, up to GRB 131004A. A cut on the probability of having a non-collapsar origin higher than 60%, estimated following Bromberg et al. (2013), was then applied, selecting a sub-sample of 12 events.

Since the spectral peak energy in this analysis is fixed to a punctual value in the source frame, the computation of the likelihood is a bit different from that in the ELF and QUSJ cases. Full details on the likelihood evaluation and the obtained results are described in Appendix A. In the following, we refer to the results of this analysis as W15*.

2.5. Priors and posterior evaluation

We chose broad priors on most parameters, considering either a uniform or a uniform-in-log distribution within a defined range for each parameter, with the following exceptions: (i) for θ_{c} and θ_{w} , we considered an isotropic prior $\pi(\theta_{\text{c/w}}) \propto \sin(\theta_{\text{c/w}})$; (ii) for the minimum luminosity of the ELF model, we chose the upper bound of the prior based on the luminosity of GRB 170817A, as stated previously; (iii) for the QUSJ model, we followed the approach of S23 to condition the prior on the observed properties of GRB 170817A (see their section 2.5.3). The bounds that we report in Table 1 refer to the priors before that conditioning. The population parameters were considered to be independent from each other, with the exceptions of (L_0, L_{**}, L_*) for the broken-power law luminosity function model and $(\theta_{\text{c}}, \theta_{\text{w}})$ for the quasi-universal structured jet model. In fact, for the triplet of luminosity breaks we imposed $L_0 < L_{**} < 10^{51} \text{ erg s}^{-1} < L_*$ while for the break angles in the quasi-universal jet structure we set $\theta_{\text{c}} < \theta_{\text{w}}$. The choice to put a boundary between L_{**} and L_* at $L = 10^{51} \text{ erg s}^{-1}$ is to avoid that those parameters to have local

Table 1. Full set of population parameters, with the associated priors.

Parameter	Prior	Description
Empirical luminosity function model		
α_{BPL}	Uniform, $\alpha_{\text{BPL}} \in [-1, 5]$	
β_{BPL}	Uniform, $\beta_{\text{BPL}} \in [0, 5]$	Slopes of the luminosity PDF in the $dP/d \ln L$ representation
γ_{BPL}	Uniform, $\gamma_{\text{BPL}} \in [-5, 5]$	
L_0	Uniform-in-log, $L_0 \in [10^{44}, 10^{47}] \text{ erg s}^{-1}$	Minimum luminosity
L_{**}	Uniform-in-log, $L_{**} \in [L_0, 10^{51} \text{ erg s}^{-1}]$	Low-luminosity break
L_*	Uniform-in-log, $L_* \in [10^{51}, 10^{56}] \text{ erg s}^{-1}$	High-luminosity break
E_p^*	Uniform-in-log, $E_p^* \in [10^2, 10^5] \text{ keV}$	Central E_p at $L = L_*$ in $L - E_p$ correlation
Quasi-universal structured jet model		
θ_c	Isotropic, $\theta_c \in [0.01, \pi/2] \text{ rad}$	Core half-opening angle
θ_w	Isotropic, $\theta_w \in [\theta_c, \pi/2 \text{ rad}]$	Structure ‘break’ angle
α_L	Uniform, $\alpha_L \in [0, 6]$	Slope of ℓ at intermediate viewing angles $\theta_c \leq \theta_v < \theta_w$
β_L	Uniform, $\beta_L \in [-3, 6]$	Slope of ℓ at large viewing angles $\theta_v \geq \theta_w$
L_c^*	Uniform-in-log, $L_c^* \in [3 \times 10^{51}, 10^{55}] \text{ erg s}^{-1}$	Typical luminosity for on-axis observers ($\theta_v = 0$)
A	Uniform, $A \in [1.5, 5]$	Slope of L_c distribution
$E_{p,c}^*$	Uniform-in-log, $E_{p,c}^* \in [10^2, 10^5] \text{ keV}$	Typical E_p for on-axis observers ($\theta_v = 0$)
α_{E_p}	Uniform, $\alpha_{E_p} \in [0, 6]$	Slope of η at intermediate viewing angles $\theta_c \leq \theta_v < \theta_w$
β_{E_p}	Uniform, $\beta_{E_p} \in [-3, 6]$	Slope of η at large viewing angles $\theta_v \geq \theta_w$
Common parameters		
y	Uniform, $y \in [-3, 3]$	$L - E_p$ correlation slope
σ_c	Uniform-in-log, $\sigma_c \in [0.3, 3]$	E_p dispersion in $L - E_p$ correlation
τ_d^{\min}	Uniform-in-log, $\tau_d^{\min} \in [0.005, 3] \text{ Gyr}$	Minimum delay between progenitor formation and SGRB
α_τ	Uniform, $\alpha_\tau \in [0, 5]$	Slope of power-law DTD
μ_τ	Uniform-in-log, $\mu_\tau \in [0.01, 5] \text{ Gyr}$	Median of the log-normal DTD
σ_τ	Uniform-in-log, $\sigma_\tau \in [0.01, 5]$	Standard deviation for the log-normal DTD
R_0	Uniform-in-log, $\sigma_c \in [1, 10^5] \text{ Gpc}^{-3} \text{ yr}^{-1}$	Short GRB local rate density

peaks in the posteriors in the same parameter region. Common parameters in the two population models share common priors. The full set of priors for each parameter with their bounds are shown in Table 1.

The posterior PDF is estimated through dynamical nested sampling, using the open source python package `dynesty` (Higson et al. 2019; Speagle 2020). The number of initial live points is set to 100 times the dimensionality of the posterior PDF, for a total of 1200 and 1400 initial live points respectively for the empirical luminosity function and the structured jet models. As stopping criteria, we chose $\text{dlogz}=0.001$ and 20000 effective samples. Batches of live points were periodically and automatically added to reach those criteria, with each batch containing one fifth of the initial live points used for the sampling.

The obtained posterior PDFs for all the cases considered are portrayed as corner plots in Appendix B, with contours representing the 90% and 50% confidence levels, while the estimated median values of the parameters with their 90% credible intervals are shown in Table 2.

3. Results

A summary of the constraints obtained on the population parameters for the ELF and QUSJ models, with both the power-law and log-normal DTDs, is given in Table 2. The results for the W15* analysis are reported in Appendix A, where we demonstrate a good agreement with the results in the original paper.

3.1. Time delay and redshift distribution

We illustrate the constraints obtained with our analyses on the shape of the rate density evolution with redshift in Fig. 1 (left-

hand panels). At each redshift z , the red (resp. blue) band shows the 90% credible range of $\dot{\rho}/R_0$ (i.e. the SGRB rate density normalized to its value at $z = 0$) for the ELF (resp. QUSJ) population model, while the yellow band shows the corresponding result from the W15* analysis. The results shown in the top row assume the power-law DTD, while those in the bottom row are for the log-normal DTD. The black curve shows the shape of the CSFH evolution of Madau & Fragos (2017), for comparison. The results are quite consistent between the ELF and QUSJ models, while the W15* analysis yields a very different constraint. The DTD parameter constraints (right-hand panels) show that this is the result of much shorter time delays in our models with respect to those obtained in the W15* analysis. To make this more evident, and to enable a comparison between different DTD models, we show in the figure, in addition to the posterior probability on the DTD parameters, also the distribution of the average time delay

$$\langle \tau_d \rangle(\mathcal{X}_{\text{pop}}) = \int \tau_d P(\tau_d | \mathcal{X}_{\text{pop}}) d\tau_d. \quad (17)$$

In the power-law DTD scenario, both luminosity function models show a steep power-law index $\alpha_\tau > 1.5$, while the minimum time delays are below $\tau_d < 350 \text{ Myr}$ (90% credible limits). The average time delays are generally below $\sim 1 \text{ Gyr}$, with median and 90% credible range of $\langle \tau_d \rangle = 160_{-143}^{+663} \text{ Myr}$ (ELF) or $\langle \tau_d \rangle = 87_{-76}^{+677} \text{ Myr}$ (QUSJ). The time delays associated to the W15* DTD parameters, on the other hand, are found to be significantly larger, yielding $\langle \tau_d \rangle = 4.0_{-2.9}^{+2.2} \text{ Gyr}$.

Similar results are obtained in the log-normal DTD case, where the median value of the log-normal distribution is $\mu_\tau < 700 \text{ Myr}$, while σ_τ is only loosely constrained to be somewhat below the upper end of its prior range, which is equivalent to 1.5

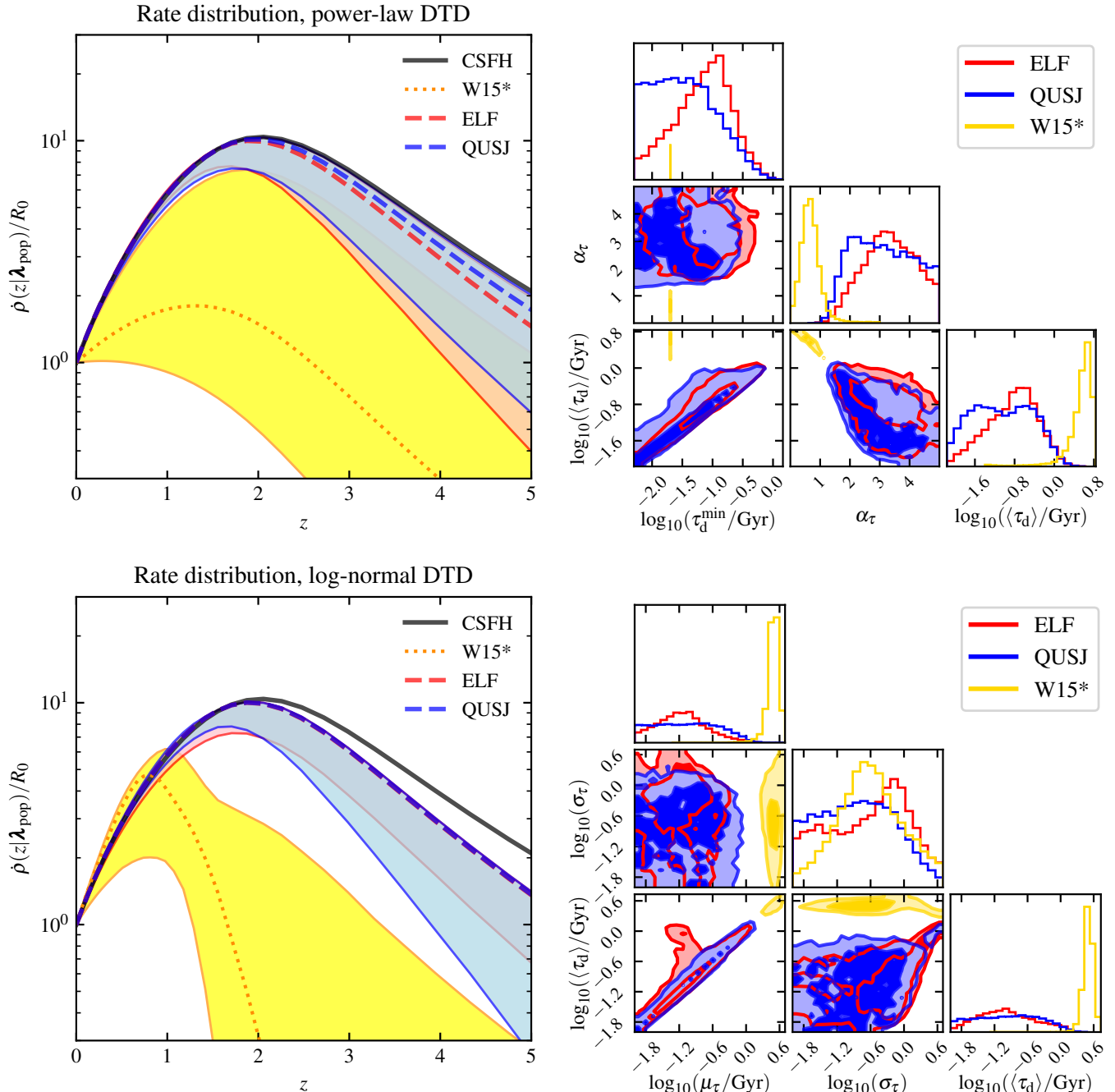


Fig. 1. Rate density distributions as functions of redshift (left panels) and corner plots of the posterior PDFs for the DTD parameters and $\langle \tau_d \rangle$ (right panels). Top and bottom panels show the results obtained with a power-law and a log-normal DTD, respectively. Rate density distributions are normalized to 1 at $z = 0$. Red and blue curves represent the distributions obtained considering, respectively, the empirical luminosity function and the quasi-universal structured jet models. **W15*** results are displayed in yellow.

dex. For both the ELF and QUSJ models, the average time delay is approximately $\langle \tau_d \rangle \sim 100^{+700}_{-80}$ Myr, while the **W15*** analysis brings $\langle \tau_d \rangle = 3.2^{+1.1}_{-1.0}$ Gyr.

3.2. Luminosity function

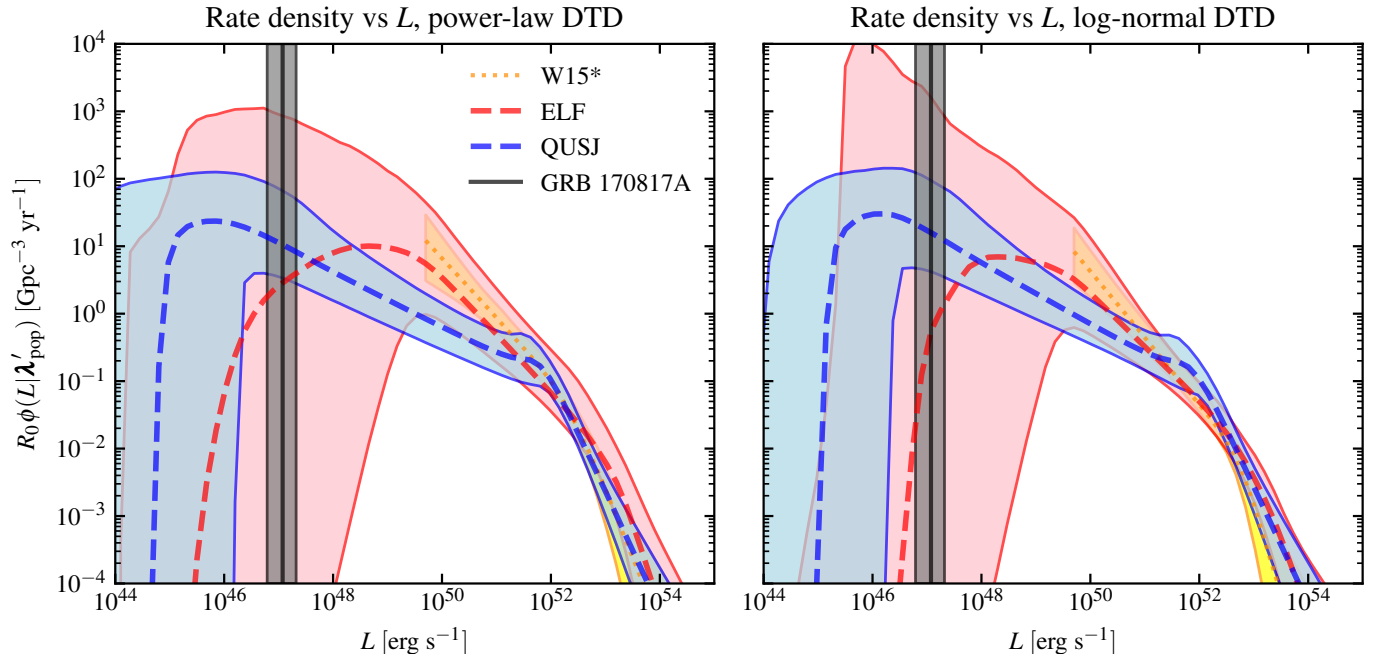
The red (resp. blue) filled areas in Figure 2 show the 90% credible bands of the luminosity function obtained assuming the ELF (resp. QUSJ) model, for the power-law DTD (left-hand panel) and the log-normal DTD (right-hand panel). In each panel, we also show in yellow the corresponding result of the **W15*** anal-

ysis. The luminosity of GRB 170817A (**S23**) is shown with a vertical grey band for comparison.

The two different DTD models considered have a limited impact on the shape of the luminosity function. Above $L_{\text{iso}} \sim 5 \times 10^{52}$ erg s $^{-1}$ both our luminosity function models show good agreement with each other and with the **W15*** results. Between $L_{\text{iso}} \sim 10^{49}$ erg s $^{-1}$ and $L_{\text{iso}} \sim 10^{52}$ erg s $^{-1}$, the trend of the ELF tends to follow the one from **W15***, while the structured jet model curves have a slightly shallower slope. This is both a result of the choice of parametrization, and also a consequence of the larger amount of information on GRB 170817A included

Table 2. Constraints on population parameters.

Empirical luminosity function			Quasi-universal structured jet		
Parameter	Power-law DTD	Log-normal DTD	Parameter	Power-law DTD	Log-normal DTD
α_{BPL}	$0.84^{+0.32}_{-0.33}$	$0.80^{+0.40}_{-0.35}$	α_L	$4.73^{+1.15}_{-1.69}$	$5.12^{+0.80}_{-1.40}$
β_{BPL}	$2.46^{+2.35}_{-1.06}$	$2.14^{+2.41}_{-0.91}$	A	$2.72^{+0.64}_{-0.37}$	$2.79^{+0.62}_{-0.40}$
γ_{BPL}	$-1.30^{+1.45}_{-3.08}$	$-1.71^{+3.89}_{-2.81}$	β_L	$3.03^{+2.59}_{-4.95}$	$1.34^{+4.25}_{-3.97}$
$\log_{10}(L_*/\text{erg s}^{-1})$	$53.03^{+0.78}_{-0.96}$	$52.76^{+0.84}_{-1.01}$	$\log_{10}(L_c^*/\text{erg s}^{-1})$	$51.73^{+0.42}_{-0.22}$	$51.75^{+0.45}_{-0.24}$
$\log_{10}(L_{**}/\text{erg s}^{-1})$	$48.81^{+1.18}_{-3.14}$	$48.35^{+1.50}_{-1.65}$			$51.70^{+0.38}_{-0.10}$
$\log_{10}(L_0/\text{erg s}^{-1})$	$44.81^{+1.53}_{-0.75}$	$45.66^{+1.22}_{-1.53}$			
$\log_{10}(E_p^*/\text{keV})$	$3.60^{+0.19}_{-0.20}$	$3.54^{+0.24}_{-0.27}$	$\log_{10}(E_{p,c}^*/\text{keV})$	$3.50^{+0.25}_{-0.28}$	$3.51^{+0.29}_{-0.28}$
			α_{E_p}	$1.30^{+0.90}_{-0.68}$	$1.45^{+0.84}_{-0.85}$
			β_{E_p}	$0.40^{+4.78}_{-3.04}$	$1.46^{+4.00}_{-4.00}$
			θ_c/deg	$2.56^{+2.55}_{-1.80}$	$3.08^{+2.03}_{-1.57}$
			θ_w/deg	$65.78^{+20.94}_{-36.40}$	$61.39^{+25.33}_{-38.05}$
			$\log_{10}(\sigma_c)$	$-0.06^{+0.08}_{-0.08}$	$-0.05^{+0.07}_{-0.08}$
			y	$0.06^{+0.29}_{-0.27}$	$0.05^{+0.32}_{-0.30}$
			$\tau_d^{\text{min}}/\text{Gyr}$	$0.03^{+0.23}_{-0.02}$	$0.0^{+0.3}_{-0.3}$
			α_τ	$3.08^{+1.70}_{-1.44}$	
			μ_τ/Gyr		$0.09^{+0.59}_{-0.07}$
			σ_τ		$0.14^{+1.59}_{-0.13}$
			$\log_{10}(R_0/\text{Gpc}^{-3}\text{yr}^{-1})$	$2.74^{+0.68}_{-0.79}$	$2.25^{+0.50}_{-0.50}$
					$2.26^{+0.67}_{-0.71}$

Notes. The S23 results refer to their ‘flux-limited sample’ analysis. All constraints are represented by their medians and 90% posterior credible intervals.**Fig. 2.** Luminosity probability distributions obtained considering either a power-law or a log-normal DTD (left and right panel, respectively). Results obtained with the broken power-law model are shown in red and the ones obtained with the structured jet model in blue, each with the shaded areas representing their 90% credible intervals. Luminosity functions from W15 are also shown in yellow. The measured luminosity for GRB 170817A is shown in gray as a reference point.

in the QUSJ model. Below $L_{\text{iso}} \sim 10^{49} \text{ erg s}^{-1}$, the empirical luminosity function model shows very large rate uncertainties compared to the structured jet scenario. This is again a consequence of the information from GRB 170817A included in that model, and in part it also reflects the stronger predictivity of the QUSJ model at low luminosity, where the minimum luminosity is set by the maximum possible viewing angle and by the slope of the apparent structure.

3.3. Local rate density

As shown in Fig. 3, the overall local rate density inferred using the ELF (red) has a larger uncertainty compared to the result using the QUSJ model (blue), regardless of the chosen DTD model (power-law DTD: dotted lines; log-normal DTD: dashed lines). This is a direct consequence of the reduced predictivity of the ELF model on the minimum SGRB luminosity compared to the QUSJ model. It is instructive to compare these rate density con-

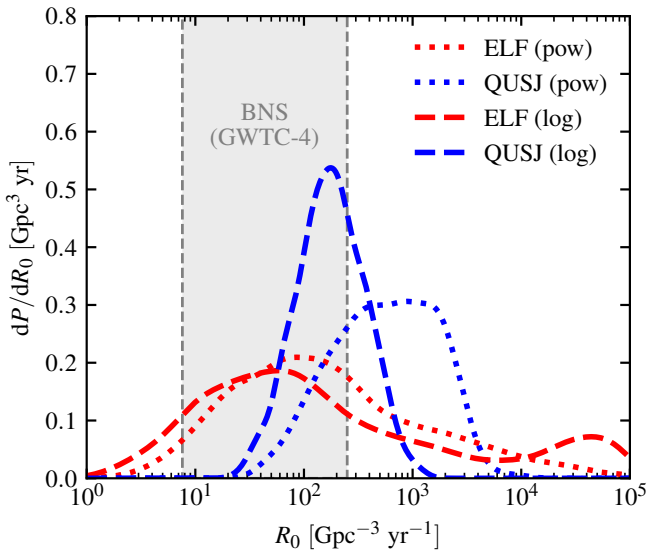


Fig. 3. Comparisons between local rate density probability distributions. Distributions obtained with the broken power-law and the structured jet luminosity models are shown in red and blue, respectively, while results corresponding to power-law and log-normal DTD are displayed respectively with dashed and dotted lines. BNS rate density inferred from GW observations (Abac et al. 2025) is shown in gray (90% credible intervals).

straints with the most recent local BNS merger rate density constraint inferred from gravitational wave observations, based on the fourth gravitational wave transient catalog (GWTC-4, Abac et al. 2025, $R_0 \in [7.6, 250] \text{ Gpc}^{-3} \text{ yr}^{-1}$ as shown by the vertical grey band in the figure). For all model choices except the QUSJ with the power-law DTD, most of the posterior support is within the GWTC-4 BNS rate density constraint. For the QUSJ model with the power-law DTD, the support is concentrated at somewhat higher local rate densities, but a substantial fraction of the probability is still within the GW constraint. In general, these results support a scenario where BNS mergers constitute the progenitors of the vast majority of SGRBs, in line with the conclusions of S23.

4. Discussion

The estimated time delays, considering all four combinations of the models considered range between $\sim 11 - 18$ Myr and $\sim 764 - 854$ Myr. The lower end of these distributions can be explained by fast BNS merger channels, which may happen in binary star systems forming with a short orbital separation and evolving quickly through a common envelope and a mass transfer phase (Tauris et al. 2017), where the merger time can further decrease thanks to neutron star natal kicks (Andrews & Zelas 2019; Beniamini & Piran 2024).

The parameter ranges found for the power-law DTD are compatible with those estimated from the Milky Way r-process element abundances (Chen et al. 2025), suggesting that BNS mergers are responsible for a significant fraction of those elements in our Galaxy.

Nonetheless, our findings for both DTD models are in contrast with time delay estimations in other short GRB population studies, like W15, Luo et al. (2022) and Tan & Yu (2020).

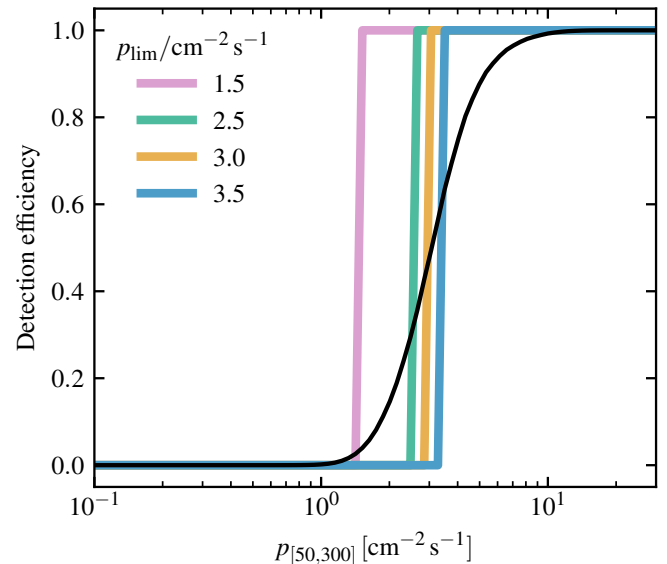


Fig. 4. Comparison between the detection efficiency in our simulated sample and that used in the inference. The black solid line shows the detection efficiency model $p_{\text{det,GBM}}$ from S23 as a function of the SGRB photon flux, assuming $E_{\text{p,obs}} = 100 \text{ keV}$. The thick coloured lines show the hard-threshold detection efficiency models assumed in our inference on the simulated sample described in Section 4.1, with different colours indicating different assumed photon flux thresholds as in Figure 5. For each of these analyses, only the SGRBs above the assumed threshold were included in the inference.

The differences could be in part traced back to the different SGRB samples with a measured redshift considered. For example, the largest measured redshift for a GRB of the W15 sample is $z = 1.131$, while our sample contains 4 GRBs with a measured redshift beyond that value, up to $z = 2.28 \pm 0.14$.

However, the different treatment of the selection effects could also play a role in the estimate of the SGRB time delays. On one hand, the chosen peak-flux thresholds for *Fermi*/GBM in W15 and Tan & Yu (2020) and for *Swift*/BAT in W15 are below the respective completeness flux thresholds. Moreover, many previous studies relied on rest-frame samples (i.e. samples of GRBs with measured redshifts) constructed without a careful assessment of their selection effects and how these could have distorted their redshift distribution. To test for the impact of incorrectly modeling the selection effects on the time delay parameters inference, we performed the additional analysis runs described below.

4.1. Explaining the longer time delays in previous studies

To demonstrate the biases deriving from using a flux-incomplete sample, we simulated a sample of short GRBs with an ELF and a power-law DTD using the following parameters: $\alpha_{\text{BPL}} = 2$, $\beta_{\text{BPL}} = 3$, $\gamma_{\text{BPL}} = 1$, $L_0 = 10^{46} \text{ erg s}^{-1}$, $L_{**} = 10^{48} \text{ erg s}^{-1}$, $L_* = 10^{52} \text{ erg s}^{-1}$, $\tau_d^{\text{min}} = 0.1 \text{ Myr}$, $\alpha_\tau = 1$, $E_p^* = 1 \text{ MeV}$, $y = 0.3$ and $\sigma_c = 1$. We considered *Fermi*/GBM as the only detector and we modeled its detection efficiency following S23. Figure 4 shows the assumed detection efficiency as a function of $p_{[50,300]}$ (black line – the plot assumes $E_{\text{p,obs}} = 100 \text{ keV}$, but the dependence on the latter parameter is weak, see S23). This allowed us to obtain a sample of 271 simulated SGRBs that were ‘detected’. We divided this sample into an observer-frame

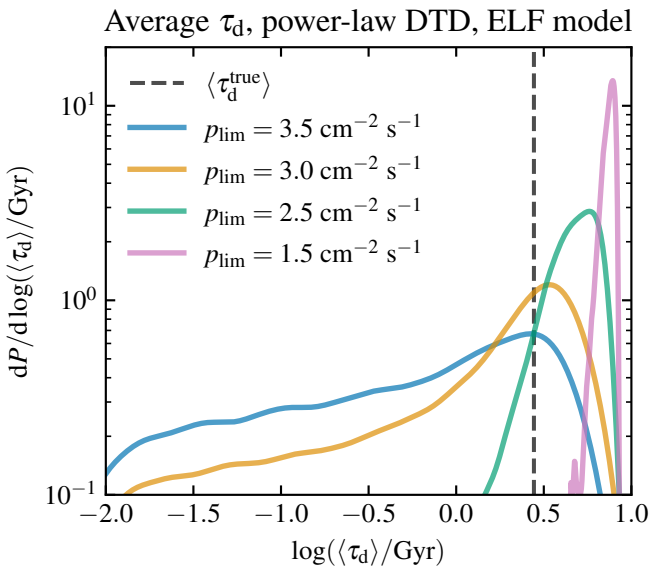


Fig. 5. Posterior distribution of the average time delay for inference on a simulated SGRB population assuming different photon peak flux cuts. The dashed black line shows the ‘true’ average time delay value corresponding to the power-law DTD parameters from which the SGRB events have been sampled. The blue curve shows the result obtained with the same flux threshold cut as in our analysis, which ensures flux completeness of the sample. The yellow, green and pink ones are obtained with lower threshold values, as reported in the legend.

and a rest-frame sample of 241 and 30 events, respectively. For the inference, we considered a hard flux threshold detection efficiency model $P_{\text{det}}(L, E_p, z) = \Theta(p_{[50,300]}(L, E_p, z) - p_{\text{lim}})$ for different values of p_{lim} , namely 3.5, 3.0, 2.5 and 1.5 $\text{cm}^{-2} \text{s}^{-1}$ (the assumed detection efficiency models are shown by the thick colored lines in Fig. 4). For each p_{lim} value considered, we ran the inference only on the subsample of simulated SGRBs brighter than that threshold.

Fig. 5 shows the posterior distribution of the average time delay for each of these four inference runs. When $p_{\text{lim}} = p_{\text{lim,GBM}} = 3.5 \text{ cm}^{-2} \text{s}^{-1}$, the sample is ‘complete’ in flux (in practice, the detection efficiency is $\gtrsim 80\%$ above the chosen threshold) and the posterior distribution peak coincides with the true value of the simulated population $\langle \tau_d^{\text{true}} \rangle = 2.78 \text{ Gyr}$. When the assumed $p_{\text{lim}} < p_{\text{lim,GBM}}$, the inference systematically overestimates the inferred time delays.

This simple simulation shows that the long time delays inferred in previous SGRB population studies are most likely due to an incorrect modeling of the selection effects, leading to their erroneous handling in the population model and to improper constructions of the SGRB flux and redshift samples.

5. Conclusions

We performed a hierarchical Bayesian study of the short GRB population in order to determine time delays between those events and the cosmic star formation history. In order to minimize observational biases, we selected both a flux-complete and a high redshift-completeness sample of SGRBs. We considered two different models for the delay time distribution, namely a power-law with a minimum time delay and a log-normal distribution, and modeled the luminosity probability distribution of our population either as a doubly broken power-law or starting

from a quasi-universal jet structure. We chose the cosmic star formation history from Madau & Fragos (2017).

The inferred parameters for a power-law delay time distribution model are compatible with the estimates from the r-process elements in our Galaxy (Chen et al. 2025) and correspond to time delays ranging from $\sim 11\text{--}17 \text{ Myr}$ to $\sim 764\text{--}823 \text{ Myr}$. The steep power-index ($\alpha_\tau > 1.5$) deviates from the ‘conventional’ value $\alpha_\tau = 1$ adopted for a binary system which evolves losing energy solely through gravitational radiation. This suggests that compact binary systems can merge through faster channels, forming for example with a low initial orbital separation and undergoing through a common envelope and mass transfer phase (Tauris et al. 2017) and, in some cases, speeding up the merger when neutron star natal kicks occur (Andrews & Zezas 2019; Beniamini & Piran 2024).

The same fast merger channel scenarios are compatible with our findings for a log-normal delay time distribution, where the expected time delays go from $\sim 13\text{--}18 \text{ Myr}$ to $\sim 816\text{--}854 \text{ Myr}$.

For each of the delay time distributions considered, we found that the choice of luminosity function model has a limited impact on the time delay results, supporting the conclusion that our finding does not depend specifically on our parametrization of the luminosity function.

We finally tested the impact of ill-modeled selection effects on the inferred time delays of a SGRB population by repeating the study for a simulated sample and using different values for its flux cut, finding that the inferred time delays are shifted towards higher values when using a flux threshold lower than the completeness one.

We therefore stress the importance of building samples whose selection effects are understood and correctly modeled in the inference, in order to minimize the observational biases when studying a population of astrophysical events.

Acknowledgements. MP acknowledges the fundings from the Fonds de la Recherche Scientifique - FNRS, Belgium, under grant No. 4.4501. OS acknowledges support from the Italian National Institute for Astrophysics (INAF) through ‘Finanziamento per la ricerca fondamentale’ grant number 1.05.23.04.04, and also funding by the European Union-Next Generation EU, PRIN 2022 RFF M4C21.1 (202298J7KT - PEACE).

References

- Abac, A. G., Abouelfettouh, I., Acernese, F., & et al. 2025, arXiv e-prints, arXiv:2508.18083
- Abbott, B. P., Abbott, R., Abbott, T. D., et al. 2017, ApJ, 848, L13
- Abbott, R., Abbott, T. D., Acernese, F., et al. 2022, ApJ, 928, 186
- Andrews, J. J. & Zezas, A. 2019, MNRAS, 486, 3213
- Band, D., Matteson, J., Ford, L., et al. 1993, ApJ, 413, 281
- Beniamini, P. & Piran, T. 2019, MNRAS, 487, 4847
- Beniamini, P. & Piran, T. 2024, ApJ, 966, 17
- Berger, E. 2014, ARA&A, 52, 43
- Bromberg, O., Nakar, E., Piran, T., & Sari, R. 2013, ApJ, 764, 179
- Burns, E., Connaughton, V., Zhang, B.-B., et al. 2016, ApJ, 818, 110
- Chen, H.-Y., Landry, P., Read, J. S., & Siegel, D. M. 2025, ApJ, 985, 154
- D’Avanzo, P., Salvaterra, R., Bernardini, M. G., et al. 2014, MNRAS, 442, 2342
- Ferro, M., Brivio, R., D’Avanzo, P., et al. 2023, A&A, 678, A142
- Ghirlanda, G., Ghisellini, G., & Celotti, A. 2004, A&A, 422, L55
- Ghirlanda, G., Salafia, O. S., Pescalli, A., et al. 2016, A&A, 594, A84
- Higson, E., Handley, W., Hobson, M., & Lasenby, A. 2019, Statistics and Computing, 29, 891
- Kouveliotou, C., Meegan, C. A., Fishman, G. J., et al. 1993, ApJ, 413, L101
- Leibler, C. N. & Berger, E. 2010, ApJ, 725, 1202
- Luo, J.-W., Li, Y., Ai, S., Gao, H., & Zhang, B. 2022, MNRAS, 516, 1654
- Madau, P. & Fragos, T. 2017, ApJ, 840, 39
- Mandel, I., Farr, W. M., & Gair, J. R. 2019, MNRAS, 486, 1086
- Maoz, D. & Nakar, E. 2025, ApJ, 982, 179
- Navia, L., Ghirlanda, G., Ghisellini, G., & Celotti, A. 2011, A&A, 530, A21
- Paul, D. 2018, MNRAS, 477, 4275
- Piran, T. 1992, ApJ, 389, L45

Planck Collaboration, Ade, P. A. R., Aghanim, N., et al. 2014, A&A, 571, A30
Salafia, O. S., Ravasio, M. E., Ghirlanda, G., & Mandel, I. 2023, A&A, 680, A45
Speagle, J. S. 2020, MNRAS, 493, 3132
Tan, W.-W. & Yu, Y.-W. 2020, ApJ, 902, 83
Tauris, T. M., Kramer, M., Freire, P. C. C., et al. 2017, ApJ, 846, 170
von Kienlin, A., Meegan, C. A., Paciesas, W. S., et al. 2020, ApJ, 893, 46
Wanderman, D. & Piran, T. 2015, MNRAS, 448, 3026
Yonetoku, D., Murakami, T., Nakamura, T., et al. 2004, ApJ, 609, 935
Zevin, M., Nugent, A. E., Adhikari, S., et al. 2022, ApJ, 940, L18

Appendix A: Likelihoods and results for W15*

Appendix A.1: Likelihood evaluation

The likelihood numerator described in Eq. 2 for the *Fermi*/GBM and *CGRO*/BATSE samples are computed in a similar way to what done in S23, but considering the photon spectral peak energy in the source frame fixed to $E_p^* = 800$ keV. We can, in fact, write the posterior probability on the source parameters like $P(\lambda_{\text{src}}|\mathbf{d}_i) = P(\mathbf{d}_i|\lambda_{\text{src}})\pi(L)\pi(z)/P(\mathbf{d}_i)$. Then, assuming that $P(\lambda_{\text{src}}|\mathbf{d}_i) \propto \pi(z)$ and neglecting the uncertainty on the measured $p_{[E_0, E_1]}$, we can write

$$P(\mathbf{d}_i|\lambda_{\text{src}}) \propto \frac{\delta(L - \hat{L}_i(z))}{\pi(L)} P(\mathbf{d}_i) \quad (\text{A.1})$$

where $\hat{L}_i(z) = L(p_i, E_p^*, z)$. We can compute the prior on L by assuming a uniform prior in $p_{[E_0, E_1]}$ and applying a coordinate transform

$$\pi(L) = \frac{\partial p_i}{\partial L} \pi(p_i) \propto \frac{p_i}{L} \quad (\text{A.2})$$

so that we obtain that the numerator for the likelihood terms in the product for each event of the sample is

$$\mathcal{N}_i^{\text{BATSE-GBM}}(\mathbf{d}_i|\lambda'_{\text{pop}}) = P(\mathbf{d}_i) \int_0^\infty \frac{\hat{L}_i(z)}{p_i} P_{\text{pop}}(\hat{L}_i(z), z|\lambda'_{\text{pop}}) dz. \quad (\text{A.3})$$

The likelihood numerator for the *Swift*/BAT sample is built in an analogous way. By neglecting the uncertainty on the measured luminosity and redshift we have

$$P(\mathbf{d}_i|\lambda_{\text{src}}) \propto \frac{\delta(L - L_i)\delta(z - z_i)}{\pi(L, z)} P(\mathbf{d}_i). \quad (\text{A.4})$$

If we assume a prior uniform in $\ln(L)$ and z , we have that $\pi(L, z) \propto L^{-1}$ and therefore the likelihood numerator for *Swift*/BAT events is

$$\mathcal{N}_i^{\text{BAT}}(\mathbf{d}_i|\lambda'_{\text{pop}}) = P(\mathbf{d}_i)L_i P_{\text{pop}}(L_i, z_i|\lambda'_{\text{pop}}) \quad (\text{A.5})$$

For the events in the three samples, the likelihood denominator can be computed like in Eq. 3

$$\mathcal{D}(\lambda'_{\text{pop}}) = \int \Theta(p_{[E_0, E_1]}(\lambda_{\text{src}}, E_p^*) - p_{\text{lim}, k}) P_{\text{pop}}(\lambda_{\text{src}}|\lambda'_{\text{pop}}) d\lambda_{\text{src}}. \quad (\text{A.6})$$

The astrophysical SGRB local rate density R_0 is estimated using the rate of observed SGRBs in the *Fermi*/GBM sample, with its corresponding $\mathcal{D}(\lambda'_{\text{pop}})$ and considering an effective observing time of $T \cdot \eta_{\text{DC}} = 3.65$ yr (W15).

Appendix A.2: Priors and posterior evaluation

The prior PDFs for the population parameters λ'_{pop} have been chosen independent between each other, i.e. $\pi(\lambda'_{\text{pop}}) = \pi(\alpha_{\text{BPL}})\pi(\beta_{\text{BPL}})\pi(L_*)\pi(\alpha_t)\pi(R_0)$ and $\pi(\lambda'_{\text{pop}}) = \pi(\alpha_{\text{BPL}})\pi(\beta_{\text{BPL}})\pi(L_*)\pi(\mu_t)\pi(\sigma_t)\pi(R_0)$ respectively for the power-law and the log-normal DTD models. All the priors have been chosen either uniform or uniform in logarithm, within the bounds that we can deduce from W15 plots. The set of priors used is listed in table A.1.

Table A.1. Population parameters for the W15 study and priors used in our test

Parameter	Prior
α_{BPL}	Uniform, $\alpha_{\text{BPL}} \in [0, 5]$
β_{BPL}	Uniform, $\beta_{\text{BPL}} \in [0, 6]$
L_*	Uniform-in-log, $L_* \in [10^{51}, 10^{53}] \text{ erg s}^{-1}$
α_t	Uniform, $\alpha_t \in [0, 3]$
μ_t	Uniform, $\mu_t \in [0.01, 5] \text{ Gyr}$
σ_t	Uniform, $\sigma_t \in [0.01, 5]$
R_0	Uniform-in-log, $R_0 \in [1, 10^5] \text{ Gpc}^{-3} \text{ s}^{-1}$

As in Sect. 2.5, the evaluation of the posterior PDF is performed through dynamical nested sampling. The number of initial live points is set to 200 times the dimensionality of the posterior PDF, for a total of 1000 and 1200 initial live points respectively for the power-law and the log-normal DTD models. As stopping criteria, we choose $\text{dlogz}=0.001$ and 20000 effective samples and batches of live points were periodically and automatically added to reach those criteria, with each batch containing one fifth of the initial live points.

Appendix A.3: Results

The obtained posterior PDF corner plots are shown in Fig. B.1 and Table A.2 shows the values estimated for the parameters of the population. Although the CSFH we used to reproduce those results (Madau & Fragos 2017) is not featured in the W15 study, its trend is very similar to the one from Planck Collaboration et al. (2014), which is one of the models used for the analysis in W15 and referred to as SFR2. We therefore take into account this set of results from W15 to compare ours. The uncertainty taken into account on the median values is 1σ as in W15, in order to make a direct comparison between the two works.

The results are quite similar to those of W15, except for a shorter median time delay and a larger variance for the log-normal DTD and the local rate density whose estimate is one order of magnitude higher than the one in W15. We attribute the difference in the estimate of R_0 to the different methods used, as in W15 they build their estimate on the fraction of non-collapsar events based on the criteria by Bromberg et al. (2013).

If we perform the same analysis with a wider range of parameters for our prior PDFs, we obtain considerably different results. In fact, if we consider an uniform prior in the interval $[-3, 5]$ for α_{BPL} and a uniform-in-log prior for L_* between $[10^{50}, 10^{54}] \text{ erg s}^{-1}$, the posterior starts to exhibit multiple local maxima as shown in Fig. B.1.

By looking at the luminosity functions obtained with these extended prior bounds (Fig. A.1), we can see that both in the power-law and the log-normal case they peak around $L_{\text{iso}} \sim 2 \times 10^{50} \text{ erg s}^{-1}$, following a single power-law trend after.

The redshift distributions obtained, displayed in Fig. A.2, present different behaviors for the two delay time distribution model. The power-law model with fixed minimum time delay brings to a considerable uncertainty in the peak of the distribution, ranging from $z \sim 0.6$ to $z \sim 1.6$ when considering a 90% credible interval. Overall the curves look a bit shifted towards lower redshift when compared to the ones obtained with the tighter parameter range. On the other hand, the curves obtained with the log-normal model and a wider parameter range have a similar behavior to what has been found in W15, within. Both before and after this peak, however, the redshift distribu-

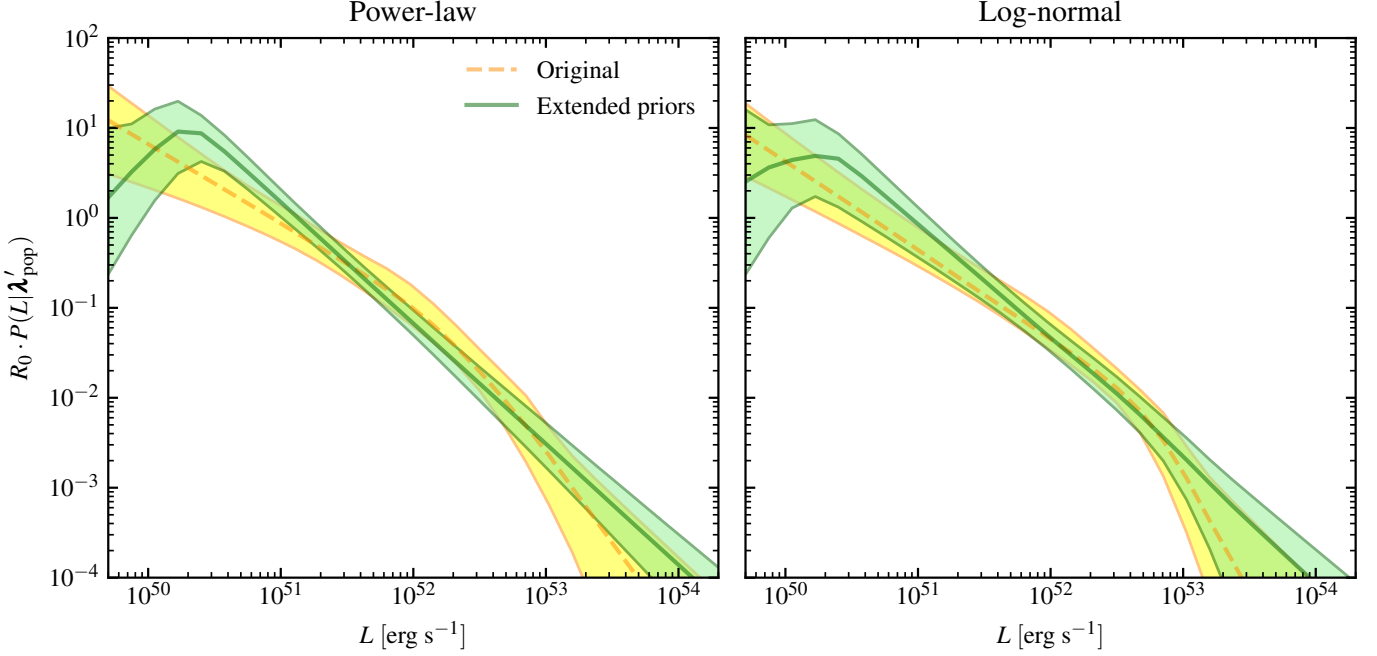


Fig. A.1. Luminosity functions obtained with the sample and model from W15, obtained considering a power-law and a log-normal DTD (respectively left and right panel). The yellow dashed curves correspond to the original parameter range considered for the study, while the green continuous curves represent the results obtained with a wider parameter range. Shaded areas depict the 90% percentiles.

Table A.2. Constraints on parameters for the W15 sample and model. Error bars depict 1σ posterior credible intervals as in W15 to make a direct comparison between the parameters inferred.

Parameter	W15 prior				Wider prior	
	Power-law		Log-normal		Power-law	Log-normal
	This work	W15 (SFR2)	This work	W15 (SFR2)	This work	
α_{BPL}	$0.88^{+0.16}_{-0.22}$	$0.90^{+0.12}_{-0.17}$	$0.98^{+0.10}_{-0.14}$	$0.96^{+0.11}_{-0.12}$	$-1.57^{+1.09}_{-0.95}$	$-0.89^{+1.93}_{-1.34}$
β_{BPL}	$1.96^{+0.89}_{-0.44}$	$2.10^{+1.10}_{-0.70}$	$2.54^{+1.58}_{-0.83}$	$1.90^{+1.00}_{-0.70}$	$1.34^{+0.10}_{-0.08}$	$1.36^{+1.73}_{-0.10}$
$\log_{10}(L_*/\text{erg s}^{-1})$	$52.20^{+0.56}_{-0.39}$	$52.30^{+0.24}_{-0.12}$	$52.62^{+0.27}_{-0.41}$	$52.30^{+0.23}_{-0.10}$	$50.32^{+0.14}_{-0.14}$	$50.38^{+2.39}_{-0.19}$
α_t	$0.65^{+0.31}_{-0.27}$	$0.71^{+0.21}_{-0.23}$			$0.47^{+0.34}_{-0.28}$	
μ_t/Gyr			$3.12^{+0.59}_{-0.60}$	$3.90^{+0.40}_{-0.50}$		$3.29^{+1.01}_{-0.96}$
σ_t			$0.24^{+0.75}_{-0.17}$	$0.00^{+0.02}_{-0.02}$		$0.87^{+1.60}_{-0.73}$
$R_0/\text{Gpc}^{-3} \text{ yr}^{-1}$	$13.8^{+7.09}_{-5.49}$	$7.7^{+5.4}_{-4.6}$	$8.51^{+4.37}_{-3.02}$	$3.6^{+1.6}_{-1.4}$	$17.38^{+6.61}_{-5.08}$	$11.22^{+5.00}_{-3.63}$

tion has a lower steepness compared to the one of the previous study.

Appendix B: Posterior PDF corner plots

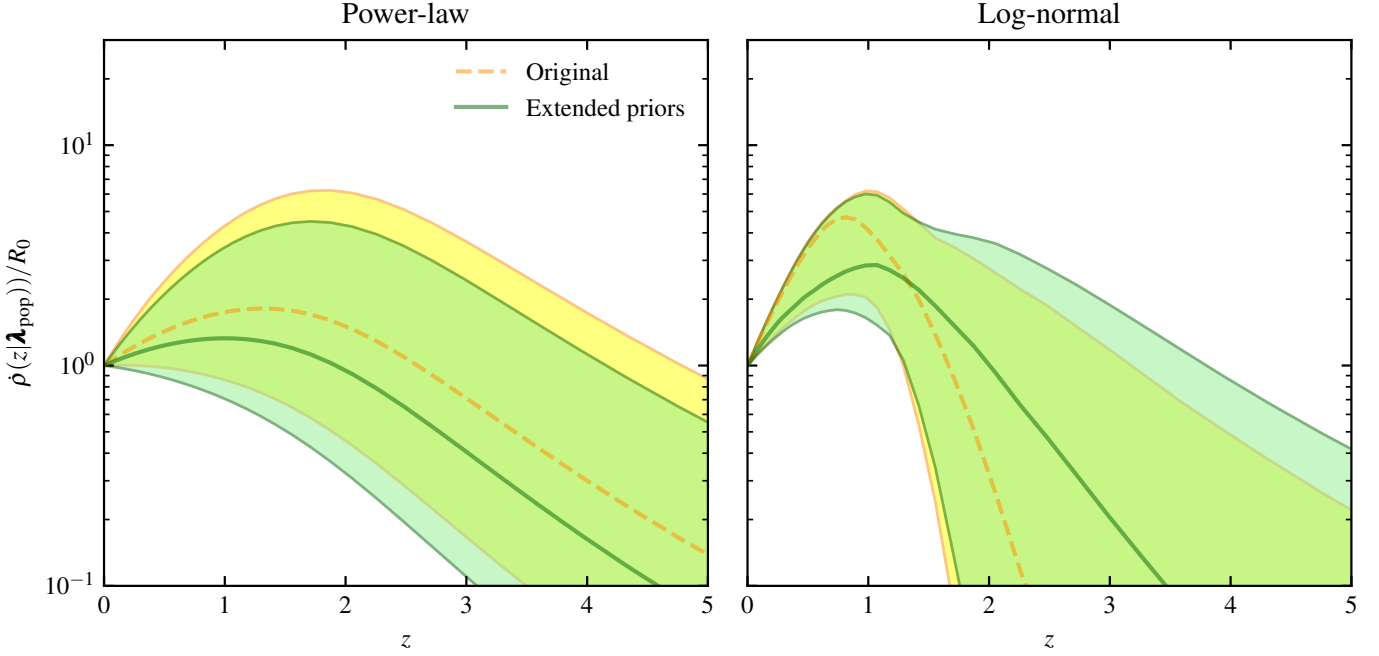


Fig. A.2. SGRB redshift distribution for the W15* population normalized to 1 at $z = 0$. The power-law and log-normal DTD scenarios are shown, respectively, in the left and right panel. The yellow dashed curves depict the original parameter range considered for the study, while the green continuous curves show the results obtained with a wider parameter range. Shaded areas correspond to the 90% percentiles.

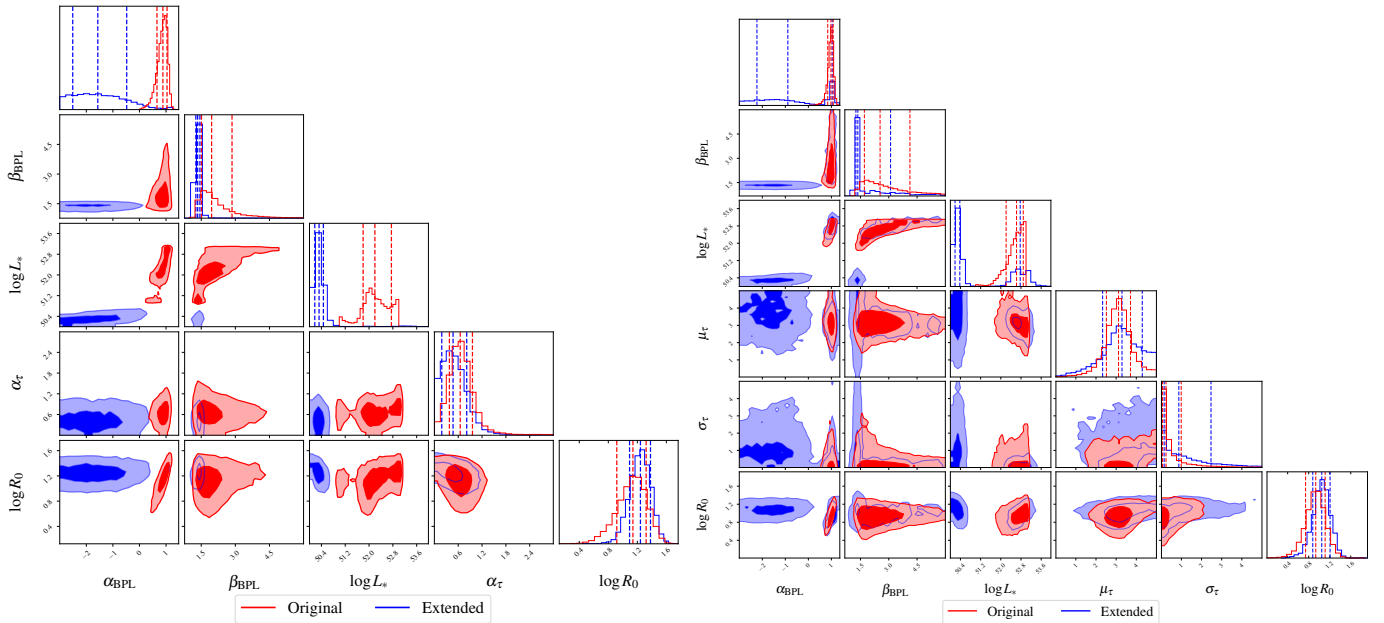


Fig. B.1. Posterior PDF contour plots for the W15* results along with the marginalized posterior PDFs on the sides for each parameter, in the power-law DTD (left panel) and log-normal DTD (right panel) cases. Red and blue contours respectively represent the results obtained using the "original" and extended priors on the parameters. Darker and lighter shades of the contours depict, respectively, the 50% and 90% confidence levels. The error bars on the marginalized posteriors mark the median of the parameters along with their 1σ uncertainty.

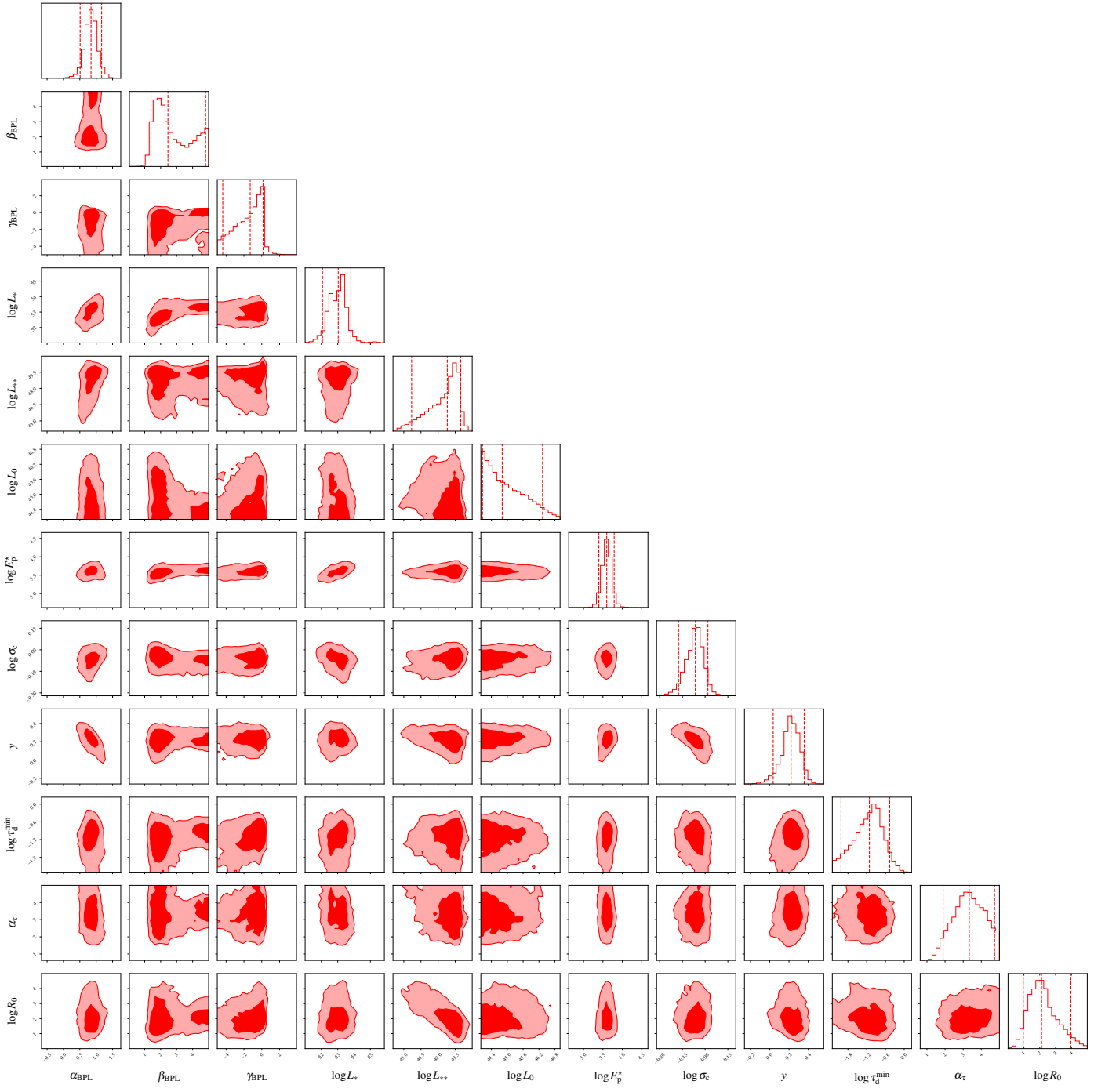


Fig. B.2. Corner plot of the posterior PDF for the ELF + power-law DTD model, with the relative marginalized posteriors for each parameter. Contours depict the 50% and 90% confidence levels. Vertical dashed lines on the marginalized posteriors represent the median values with the 90% credible intervals.

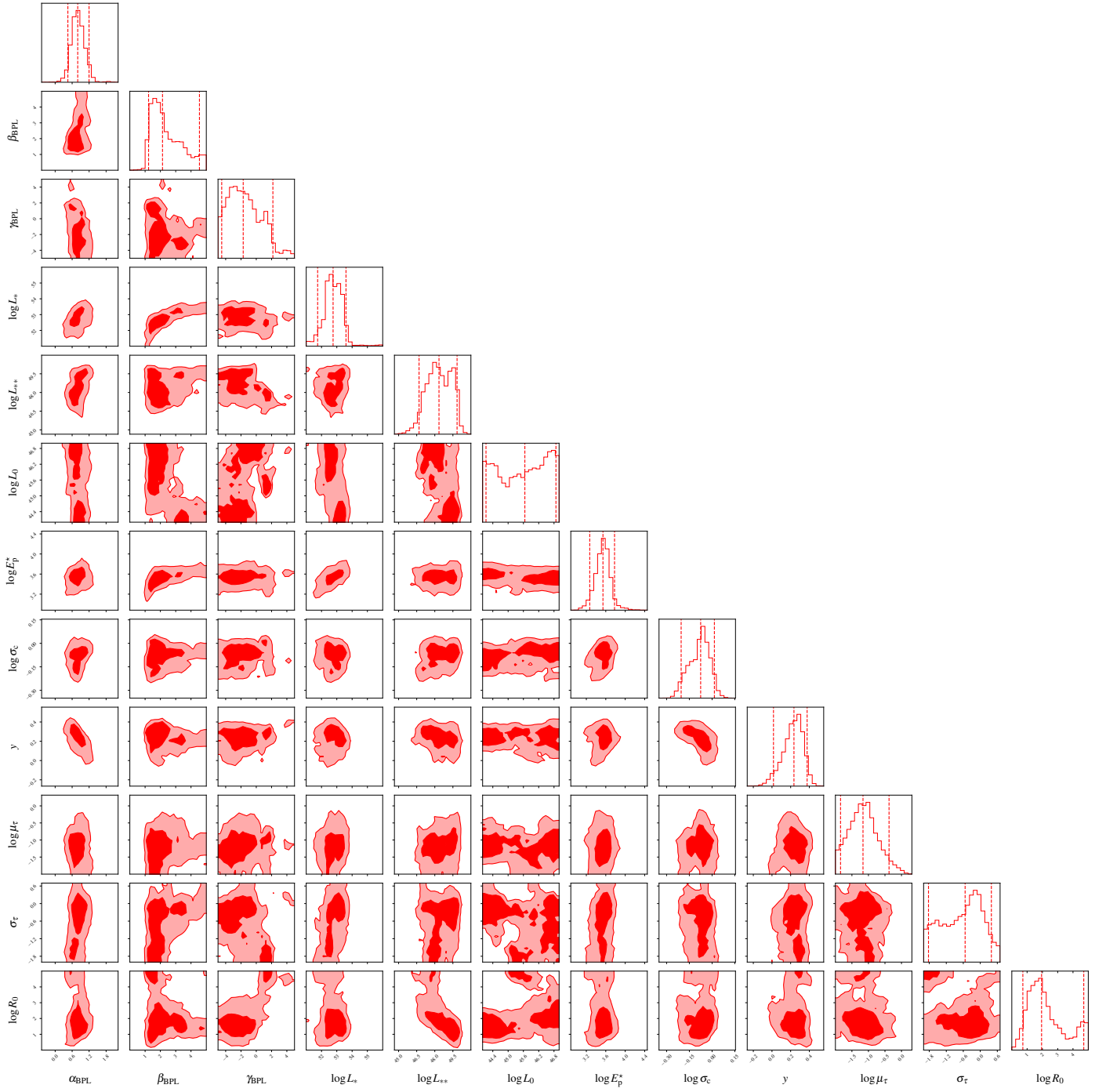


Fig. B.3. Corner plot of the posterior PDF for the ELF + log-normal DTD model, with the relative marginalized posteriors for each parameter. Contours depict the 50% and 90% confidence levels. Vertical dashed lines on the marginalized posteriors represent the median values with the 90% credible intervals.

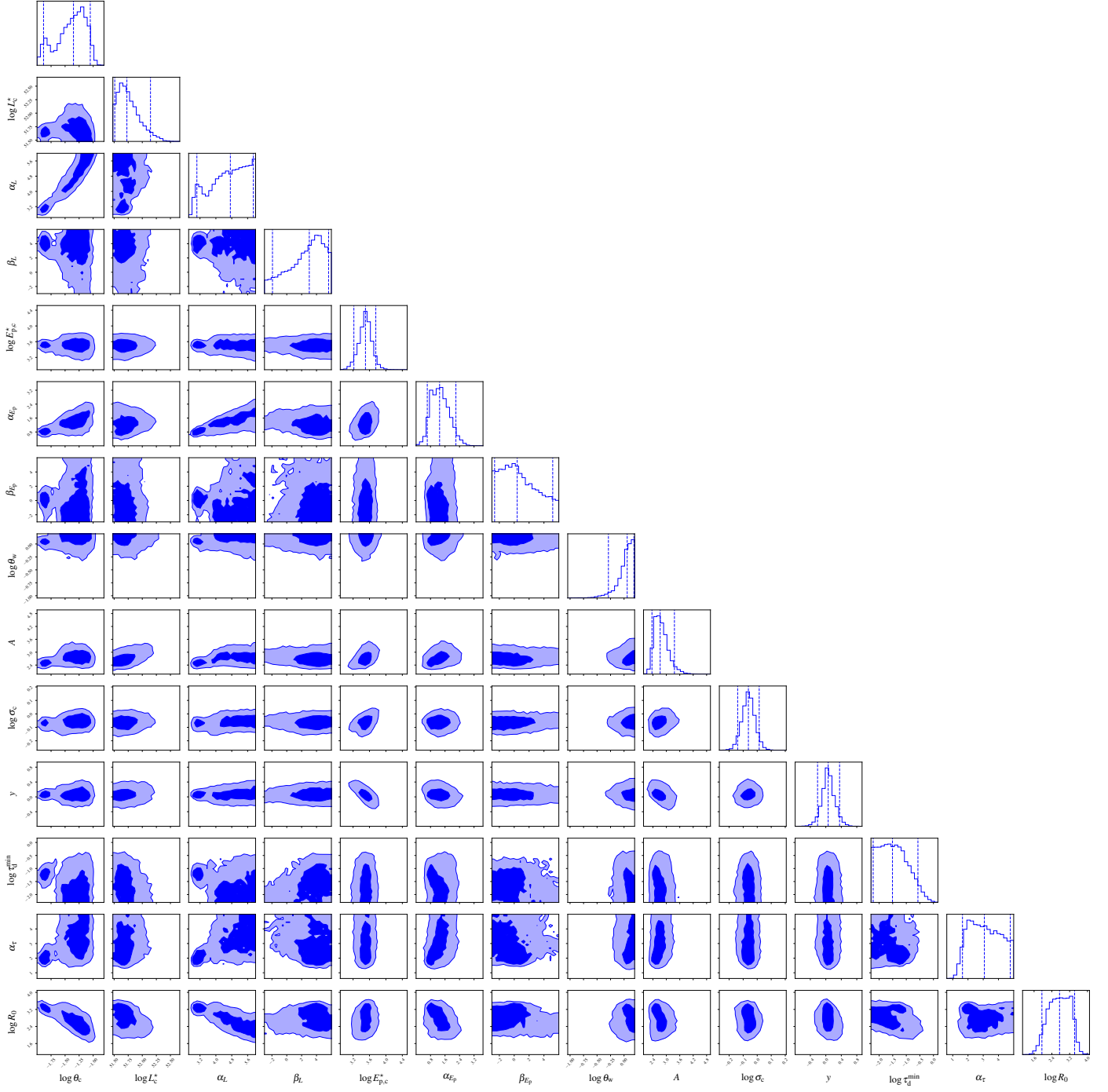


Fig. B.4. Corner plot of the posterior PDF for the QUSJ + power-law DTD model, with the relative marginalized posteriors for each parameter. Contours depict the 50% and 90% confidence levels. Vertical dashed lines on the marginalized posteriors represent the median values with the 90% credible intervals.

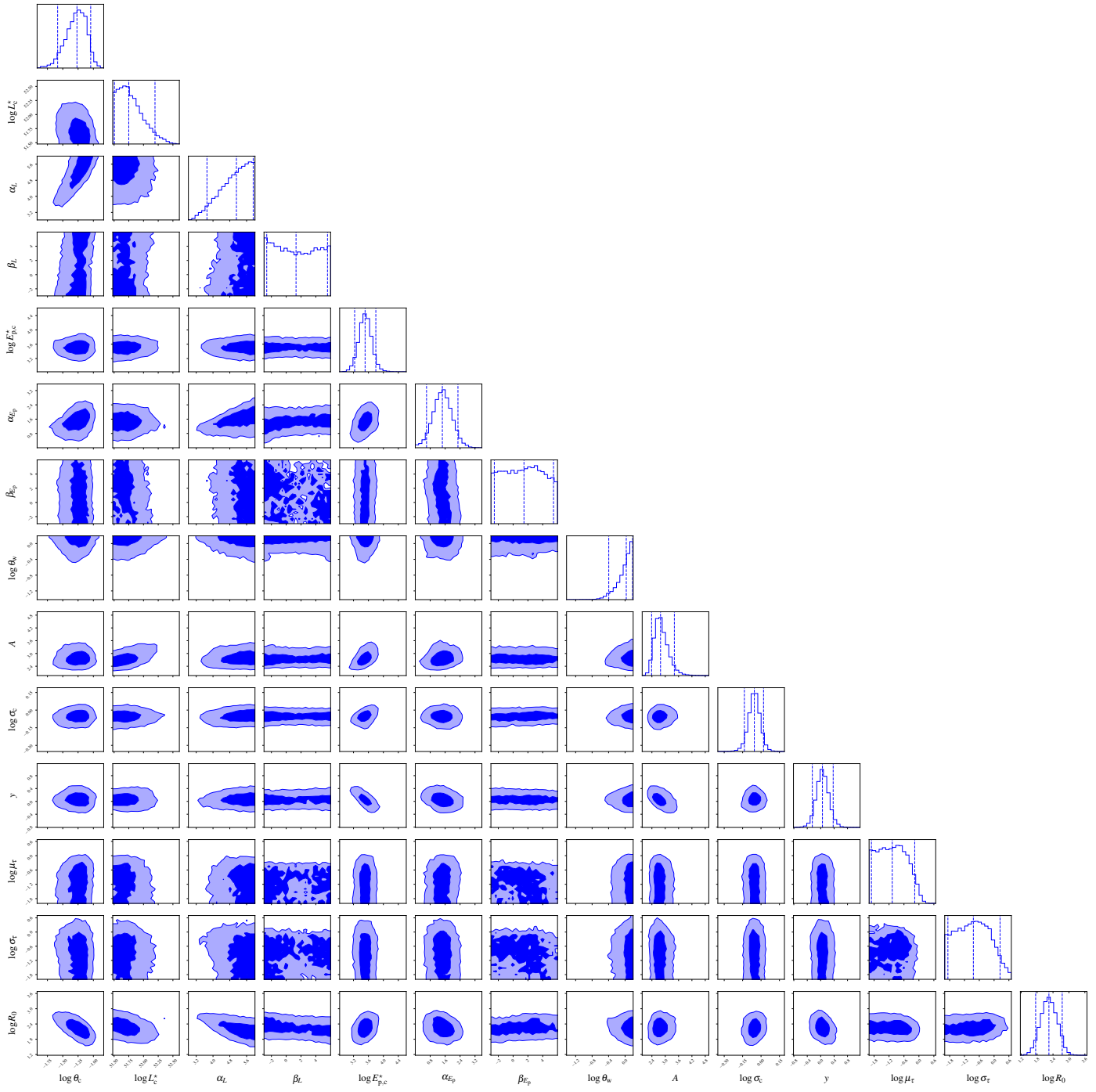


Fig. B.5. Corner plot of the posterior PDF for the QUSJ + log-normal DTD model, with the relative marginalized posteriors for each parameter. Contours depict the 50% and 90% confidence levels. Vertical dashed lines on the marginalized posteriors represent the median values with the 90% credible intervals.